Journal of Materials Chemistry B

ROYAL SOCIETY OF CHEMISTRY

PAPER

View Article Online
View Journal

Cite this: DOI: 10.1039/d5tb01048a

Near infrared-triggered diketopyrrolopyrrole nanoparticles for photothermal applications against bacterial infections

Qijia Sun,[a] Xijia Zhou,[a] Ke Wang,*[a] Tingting Sun *[b] and Zhigang Xie [b]

Received 3rd May 2025,
Accepted 19th July 2025

DOI: 10.1039/d5tb01048a

rsc.li/materials-b

Wound infection caused by bacteria is an important factor that affects the rapid healing of wounds, and the emergence of drug-resistant strains complicates the treatment, which poses great challenges to surgeons. Therefore, we synthesized a DPP derivative (DPP-S) featuring a donor–acceptor–donor (D–A–D) structure. Through the introduction of thione groups, this derivative exhibits near-infrared (NIR) absorption and excellent photothermal performance under NIR laser irradiation. DPP-S-mediated phototherapy can effectively inhibit and destroy *Staphylococcus aureus* and *Escherichia coli* biofilms and methicillin-resistant *Staphylococcus aureus* biofilms. In a mouse wound infection model, DPP-S-mediated photothermal therapy can effectively fight bacterial infection, promote the formation of new blood vessels and the deposition of collagen fibers, and thus accelerate wound healing. This discovery is of great significance for the development of new photothermal agents and provides a new direction and possibility for the treatment of clinical infectious diseases.

Introduction

In surgical patients, wound infection and poor wound healing are often caused by various bacteria and have become one of the major problems faced by clinicians.[1,2] Although antibiotics are the first choice for the treatment of bacterial infections, there are limitations in their clinical applications, such as side effects and lack of specificity. More seriously, due to the widespread use of antibiotics, many bacteria gradually develop resistance, making conventional antibiotics ineffective.[3–5] The emergence of drug-resistant bacteria complicates the treatment of common infections and leads to increased healthcare costs and poor patient outcomes. Therefore, it is particularly important to develop novel antimicrobial treatments to replace conventional antibiotics.

Researchers have proposed a series of antibiotic replacement strategies, including photodynamic therapy (PDT),[6,7] photothermal therapy (PTT),[8–10] gas therapy,[11] photocatalytic therapy,[12] sonodynamic therapy,[13,14] and combination therapies. The high temperature generated by PTT leads to the denaturation of nucleic acids and proteins as well as cell lysis, which can effectively destroy the complete structures of bacteria, making it easier for antibacterial agents to penetrate and eradicate the bacteria. In addition, PTT can prevent bacteria from developing drug resistance through metabolic regulation or the proton pump pathway because it can act on multiple cellular components simultaneously, making it difficult for bacteria to develop drug resistance.[15–18] Studies have shown that PTT can also induce a 'hot spring effect' in local tissues, promoting the proliferation and differentiation of fibroblasts and endothelial cells, thus benefitting the formation of new blood vessels and the healing of wound tissues.[19–22]

Photothermal agents (PTAs) play a crucial role in PTT. Researchers have worked to develop PTAs with NIR absorption, as the NIR laser easily penetrates tissues and is less absorbed by water and hemoglobin.[23–25] Diketopyrrolopyrrole (DPP) is a small-molecule organic dye that has attracted the attention of researchers due to its several favorable characteristics, including its excellent photophysical properties, tunable structures, and excellent photostability.[26–29] As a π-conjugated organic molecule with an endocannabinoid structure, DPP is capable of forming a donor–acceptor–donor structure, which enables the flexible tuning of its photophysical properties.[30–34] Certain DPP derivatives exhibit intrinsic advantages, including NIR absorption and robust fluorescence emission, which render them highly promising in phototherapy and fluorescence imaging (FLI).[35] Consequently, DPP derivatives demonstrate significant scientific value and potential in phototherapy applications.

In this study, dithiopheneboronic acid was chosen as the electron donor to facilitate the electron transfer of DPP,

[a] Department of Respiratory and Critical Care Medicine, The Second Hospital of Jilin University, Changchun, Jilin 130041, P. R. China
[b] Key Laboratory of Polymer Ecomaterials, Changchun Institute of Applied Chemistry, Chinese Academy of Sciences, Changchun, Jilin 130022, P. R. China

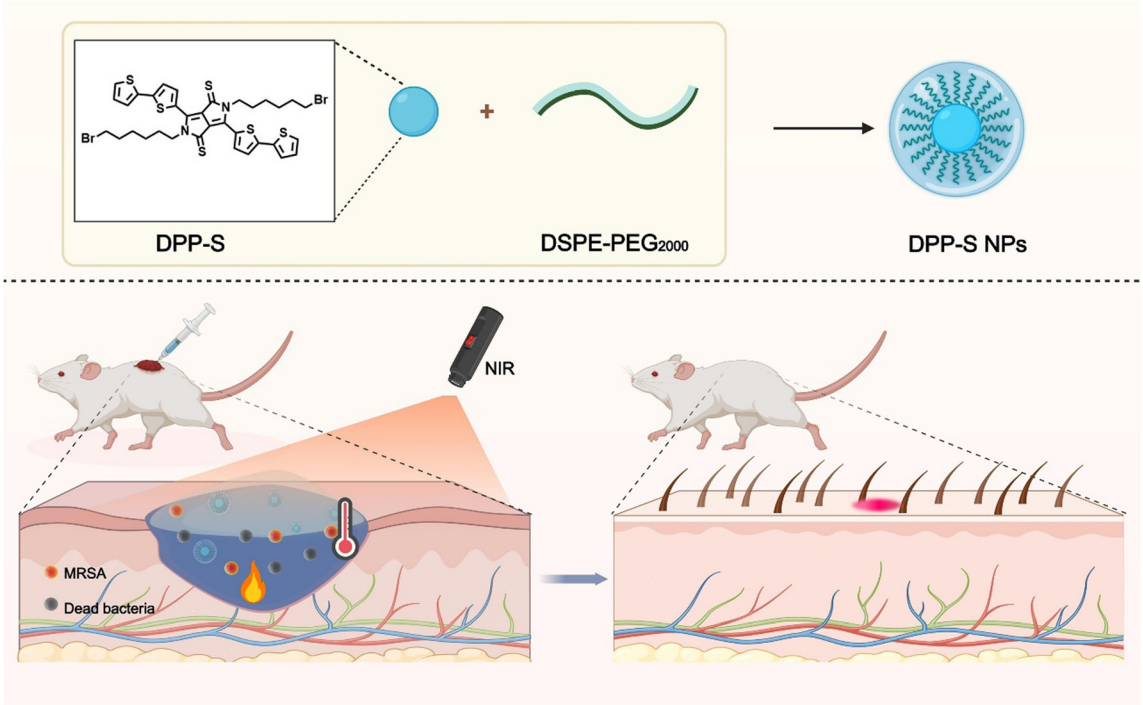

Scheme 1 Schematic representation of the antimicrobial application of DPP-S NPs.

resulting in the successful synthesis of DPP3. For further experiments on the red shift of the absorption spectrum of DPP3, the carbonyl group was subjected to a thiolation reaction, leading to the final synthesis of DPP-S. DPP-S was then encapsulated in distearoylphosphatidylethanolamine-polyethylene glycol 2000 ($DSPE\text{-}PEG_{2000}$) to form nanoparticles (DPP-S NPs) for evaluation of its therapeutic efficacy against infection (Scheme 1). Three common clinical pathogenic strains (*Staphylococcus aureus* (*S. aureus*), *Escherichia coli* (*E. coli*), and methicillin-resistant *S. aureus* (MRSA)) were selected. Under NIR laser irradiation, the nanoparticles demonstrated excellent photothermal effects and efficiently inhibited the growth of bacteria. In the wound infection model of mice, bacterial proliferation was markedly suppressed by DPP-S-mediated PTT treatment, while the formation of new blood vessels and collagen fibers was significantly enhanced, thereby expediting wound healing.

Result and discussion

Preparation and characterization of NPs

The synthesis of DPP-S involves five steps (Fig. S1). The intermediates DPP1 and DPP2 were first synthesized according to a predetermined method,[36] followed by reaction with dibenzothiophene boronic acid to obtain DPP3. Then, DPP3 was reacted with 2,4-bis(4-methoxylphenyl)-1,3-dithia-2,4-diphosphetane-2,4-disulfide (Lawesson's reagent, LR) to generate the final product DPP-S. The molecular structures of DPP3 and DPP-S were confirmed using ^{1}H NMR spectra (Fig. S2 and S3). The DPP-S structure was further characterized through ^{13}C NMR (Fig. S4) and mass spectrometry (MS) (Fig. S5). Compared with DPP3, the absorption spectrum of DPP-S shows an obvious redshift (Fig. S6). $DSPE\text{-}PEG_{2000}$ was utilized to prepare DPP-S NPs *via* a nanoprecipitation method. DPP-S NPs have a broader absorption spectrum compared with DPP-S (Fig. 1(a)). Transmission electron microscopy (TEM) results show that DPP-S NPs have a regular spherical shape (Fig. 1(b)). Dynamic light scattering (DLS) analysis shows that the average diameter of DPP-S NPs is 147.0 nm (Fig. 1(c)) with a polydispersity index (PDI) of 0.18. The zeta potential of DPP-S NPs was measured at −2.33 mV (Fig. S7). Furthermore, the particle size and PDI of DPP-S NPs in an aqueous solution remained stable over a 14-day monitoring period (Fig. 1(d)), demonstrating good colloidal stability. The electron density distributions of the highest occupied molecular orbital (HOMO) and lowest unoccupied molecular orbital (LUMO) of DPP-S with a corresponding band gap of 2.13 eV are shown in Fig. 1(e).

Photothermal performance of DPP-S NPs

The photothermal performance of DPP-S NPs was explored under 730 nm laser irradiation. After 10 min of irradiation at a laser power density of 0.6 W cm^{-2}, the temperature of water only increased by 5.6 °C, while the temperature increase (ΔT) of the DPP-S NPs at a concentration of 80 μg mL^{-1} reached 43.3 °C. Moreover, the temperature changes were closely related to the concentrations of DPP-S NPs. As shown in Fig. 2(a), under the same laser irradiation conditions, DPP-S NPs at different concentrations exhibit obvious temperature differences. In addition, the temperature increase of DPP-S NPs is related to the laser power density. As shown in Fig. 2(b), when

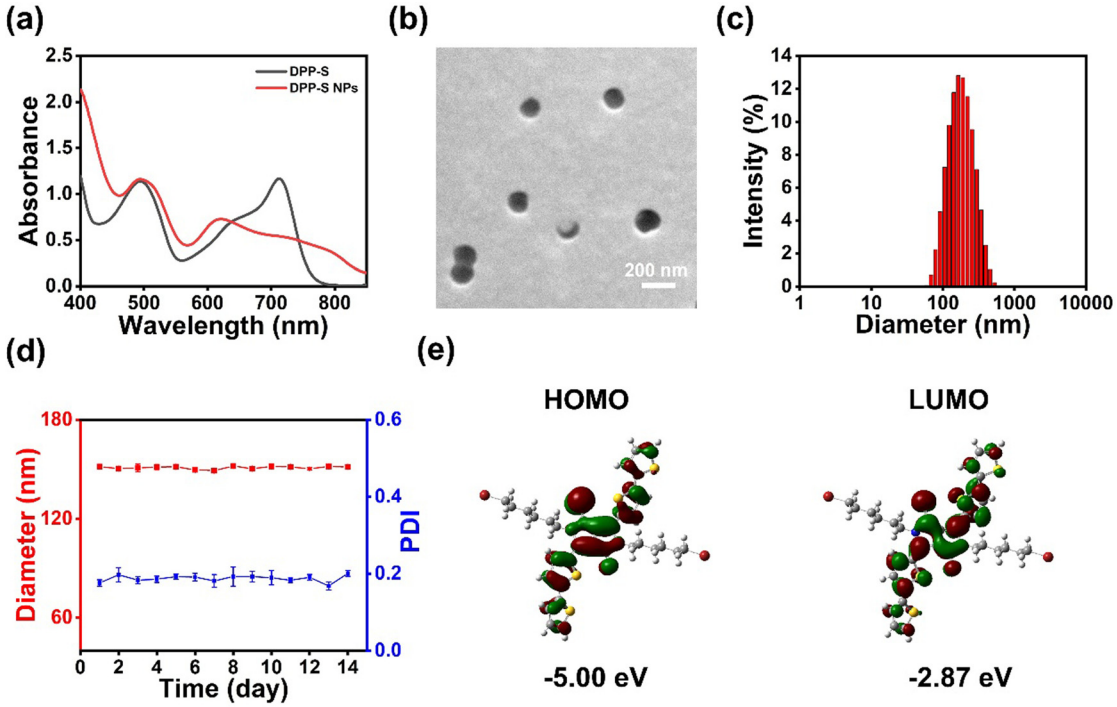

Fig. 1 Characterization of DPP-S NPs. (a) Absorption spectra of DPP-S in *N*,*N*-dimethylformamide and DPP-S NPs in water. (b) TEM image of DPP-S NPs. (c) Size distribution of DPP-S NPs characterized *via* DLS analysis. (d) Changes in the sizes and PDIs of DPP-S NPs after storage in water for 14 days. (e) HOMO–LUMO energy level diagrams of the corresponding units of the DPP-S.

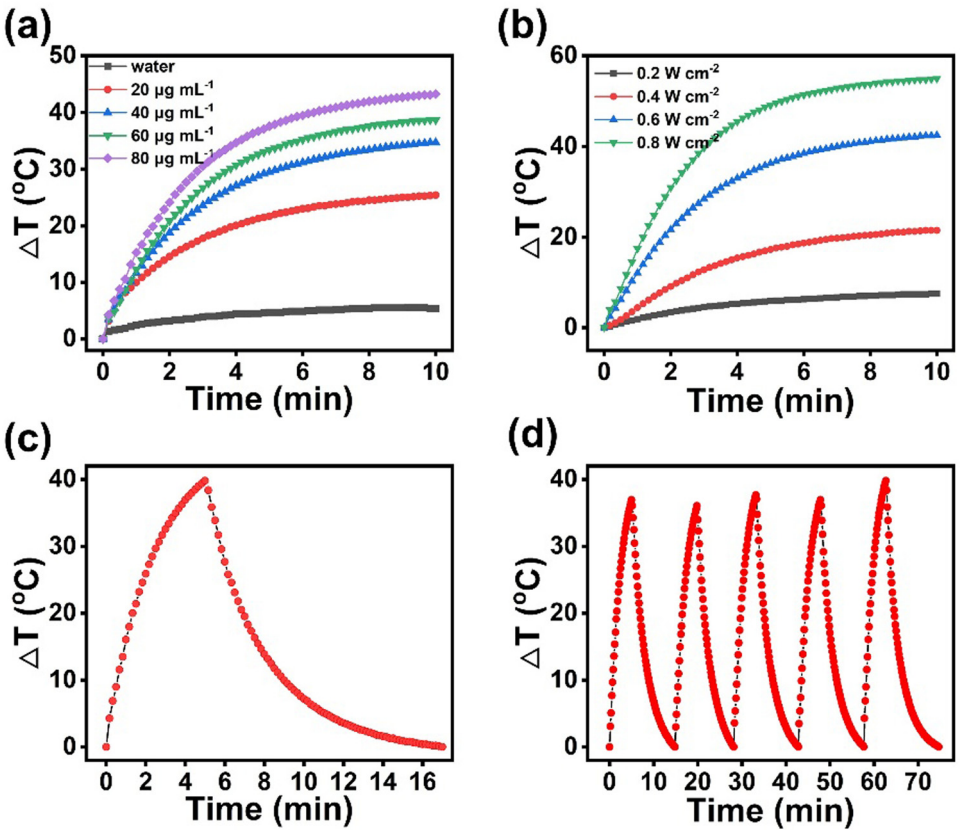

Fig. 2 Photothermal properties of DPP-S NPs. (a) Temperature changes of DPP-S NPs at different concentrations. (b) Temperature variations of DPP-S NPs under irradiation of different laser power densities. (c) Heating and cooling curve of DPP-S NPs. (d) 5 cycles of irradiation and cooling.

the concentration of DPP-S NPs is 80 μg mL^{-1}, ΔT gradually increases as the laser power density increases. Using the photothermal cooling curve, we calculated the PCE of DPP-S NPs as 38.7% (Fig. 2(c) and Fig. S8). The temperature of the DPP-S NP solution reached its initial value after five cycles, whereas that of the control ICG solution substantially decreased following multiple irradiation treatments (Fig. 2(d) and Fig. S9). This performance demonstrates the excellent photothermal stability of DPP-S NPs. The above results reveal that DPP-S NPs have excellent photothermal performance, which demonstrates their feasibility in the treatment of bacterial infections.

In vitro antibacterial performance of DPP-S NPs

The excellent photothermal properties of DPP-S NPs prompted us to investigate their antibacterial effects. First, we selected *S. aureus* and *E. coli* to evaluate their antibacterial effects. The minimum inhibitory concentration (MIC) of DPP-S NPs under laser irradiation was 60 μg mL^{-1} toward both bacteria (Fig. 3(a), (b) and Fig. S10). In addition, when the bacterial suspensions were spread on agar plates after different treatments, almost no colonies existed in the DPP-S NP-combined-laser (NPs(+)) group, indicating that the NPs can effectively kill *S. aureus* and *E. coli* under laser irradiation (Fig. 3(c)). These preliminary results demonstrate that DPP-S NPs combined with laser irradiation could effectively

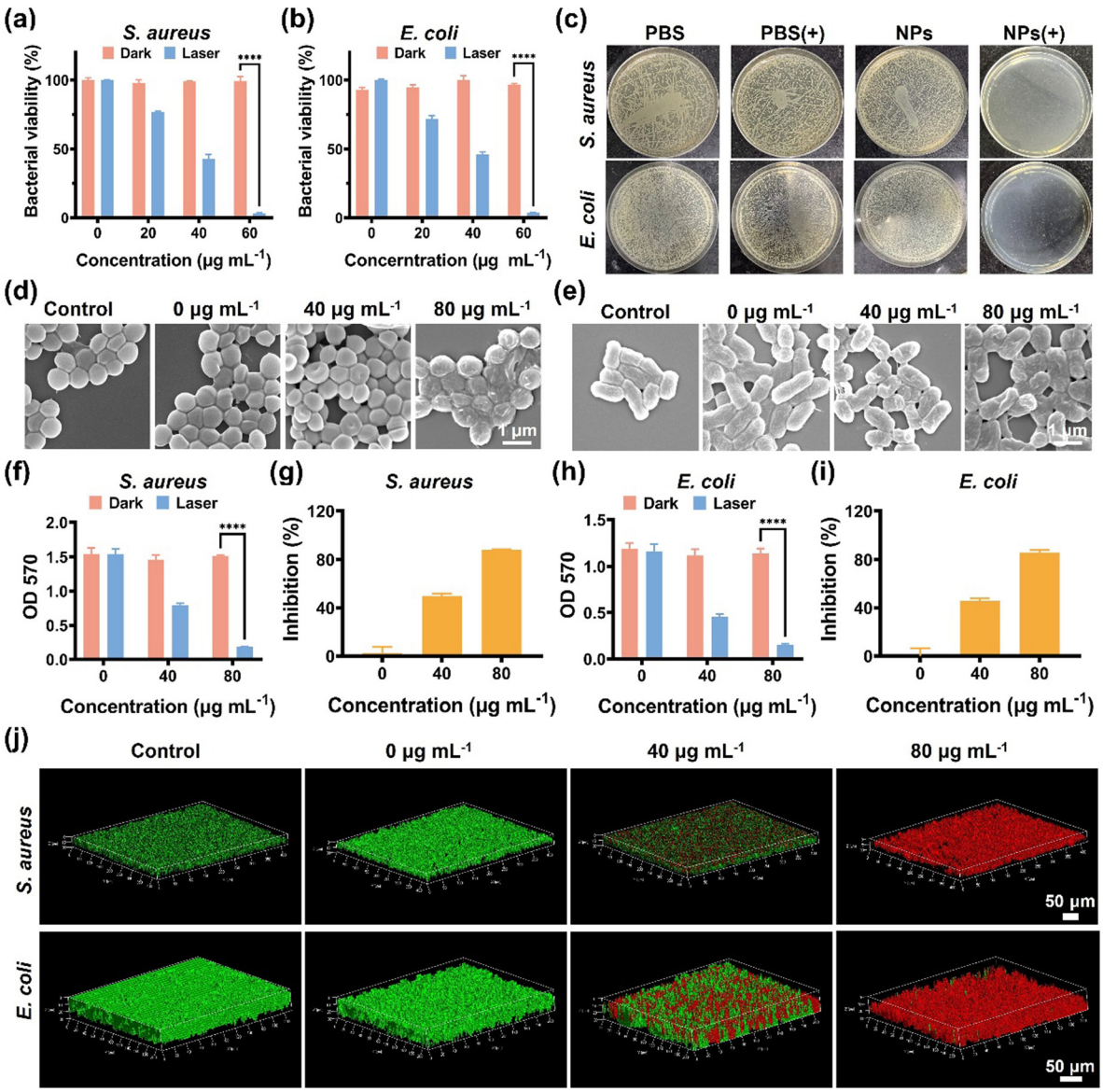

Fig. 3 *In vitro* antimicrobial effects of DPP-S NPs. Survival rates of (a) *S. aureus* and (b) *E. coli* treated with different concentrations of DPP-S NPs under different conditions. (c) Images of representative agar plates of *S. aureus* and *E. coli* after different treatments. SEM images of (d) *S. aureus* and (e) *E. coli* after different treatments. OD570 values of (f) *S. aureus* and (h) *E. coli* after different treatments. Biofilm inhibition of (g) *S. aureus* and (i) *E. coli* treated with different concentrations of DPP-S NPs after laser irradiation. (j) 3D confocal laser scanning microscopy images of *S. aureus* and *E. coli* biofilms after different treatments.

inhibit bacterial growth and kill bacteria at a certain concentration. Scanning electron microscopy (SEM) was then used to observe the bacterial morphological changes in the different treatment groups. *S. aureus* and *E. coli* in the control group showed regular round or rod-like structures, whereas the morphology of the bacteria appeared to be wrinkled and deformed with an increase in the concentration of DPP-S NPs (Fig. 3(d) and (e)).

A biofilm is a membrane structure composed of various substances that can effectively protect bacteria from adverse external factors, such as antibiotics.[37,38] The internal structure of the biofilm, rich in enzymes and small molecular substances, provides a stable living environment for bacteria.[39] Therefore, the inhibition and destruction of bacterial biofilms are key steps in antibacterial treatment. We evaluated the inhibitory activity of DPP-S NPs at different concentrations (0, 40, and 80 μg mL^{-1}) on *S. aureus* and *E. coli* biofilms under laser irradiation using crystal violet staining. As shown in Fig. S11, the biofilm in the control group was thick and relatively intact, whereas that in the NPs(+) group thinned and gradually disappeared with increasing concentration of the nanoparticle solution. The OD570 value of the crystal violet staining solution was consistent with the aforementioned results (Fig. 3(f)). When DPP-S NPs were combined with laser irradiation, the inhibition rate of the 40 μg mL^{-1} nanoparticle solution against the *S. aureus* biofilm was only 49.8%, while the biofilm inhibition rate of the 80 μg mL^{-1} nanoparticle solution against *S. aureus* was 88.1% (Fig. 3(g)). Similarly, biofilm formation inhibition was achieved against *E. coli* (Fig. 3(h) and (i) and Fig. S11).

Furthermore, the efficacy of DPP-S NP-mediated phototherapy against mature biofilms was continuously verified through live/dead bacterial staining. The three-dimensional (3D) structure of the biofilm showed that both *S. aureus* and *E. coli* in the control group exhibited distinct green fluorescence. At a concentration of 40 μg mL^{-1} of DPP-S NPs (Fig. 3(j)), a mixed fluorescence of red and green was observed, indicating that a significant number of viable bacteria were still present. When the concentration reached 80 μg mL^{-1}, most bacteria in the biofilm were dead (Fig. 3(h)). To quantitatively confirm these findings, the total bacterial colony counts in the post-treatment suspension was determined using the standard plate counting method. The results show good agreement with the aforementioned fluorescence staining observations (Fig. S12). This implies that DPP-S NPs can effectively disrupt mature biofilms. These results indicate that DPP-S NP-mediated phototherapy can effectively inhibit and destroy bacterial biofilms.

Currently, most clinically detected *S. aureus* strains are drug-resistant, especially MRSA with broad-spectrum resistance.[40] Motivated by previous experiments, we further evaluated the antibacterial performance of DPP-S NPs against MRSA. As shown in Fig. 4(a), the bacterial survival rate does not change much under dark conditions. However, under laser conditions, as the concentration of DPP-S NPs increases, the survival rate of MRSA gradually decreases, indicating that DPP-S NPs combined with laser irradiation are also effective against MRSA. Additionally, the MIC of DPP-S NPs against MRSA was determined to be 60 μg mL^{-1} (Fig. 4(a) and Fig. S10). When the bacterial solutions were spread on agar plates after different treatments, the NPs(+) group killed the bacteria, confirming their antibacterial properties against MRSA (Fig. 4(b)). SEM results of the NPs(+) group showed obvious crumpling and deformation, which also supported the above conclusion (Fig. 4(c)).

Next, we measured the inhibitory activity of DPP-S NPs against MRSA biofilms. When the concentration of DPP-S NPs reached 80 μg mL^{-1}, the absorbance of the crystal violet staining solution at 570 nm was significantly lower than that for the control group, with an inhibition rate of 72.7% (Fig. 4(d), (e) and Fig. S13). Live/dead staining experiments and semiquantitative analysis of residual bacteria in the biofilms demonstrated that DPP-S NP-mediated PTT effectively disrupted mature MRSA biofilms and killed bacteria (Fig. 4(g, f)). Altogether, DPP-S NPs combined with laser irradiation can effectively inhibit and destroy *S. aureus*, *E. coli*, and MRSA biofilms, demonstrating the broad-spectrum antimicrobial activity of DPP-S NPs.

In vivo antimicrobial effect

Considering the *in vitro* antibacterial activities of DPP-S NPs, we evaluated their therapeutic efficacy in a mouse wound infection model. Fig. 5(a) indicates that the temperature of the wounds in the NPs(+) group exceeded 55 °C during irradiation. In contrast, the wound temperature in the PBS-combined-laser irradiation group (PBS(+)) only increased to about 35 °C. Photographs were taken to record the changes in the wounds (Fig. 5(b)), and the wound trajectory was simulated using ImageJ software (Fig. 5(c)). Pronounced wrinkling and scabbing of wounds in the NPs(+) group were observed on the first day post-treatment, and the wound healing rate reached 95.8% by the 7th day (Fig. 5(d)). Furthermore, residual bacteria cultures revealed that the bacterial colony counts in the NPs(+) group were significantly lower than those in the other three groups (Fig. 5(e)).

H&E staining of the wound tissues in different treatment groups demonstrated that the NPs(+) group exhibited minimal inflammatory cell infiltration alongside a substantial number of newly formed hair follicles (Fig. 5(f)). Masson staining analysis of the wounds after treatments illustrated considerable collagen fiber deposition within the wounds in the NPs(+) group, characterized by a well-organized skin epidermis and dermis with reduced inflammatory cell infiltration (Fig. 5(f)). Additionally, CD31 fluorescence intensity markedly increased in NPs(+)-treated wounds, suggesting a significantly higher vascular density (Fig. 5(f)). Collectively, these findings suggest that DPP-S NP-mediated photothermal therapy accelerates wound healing and provides a unique advantage in the treatment of bacterial wound infections.

In vitro and *in vivo* biosafety assessment

To evaluate *in vitro* cytotoxicity, mouse fibroblast (L929) and mouse embryonic fibroblast (NIH 3T3) cells were selected and tested using 3-(4,5-dimethylthiazol-2-yl)-2,5-diphenyltetrazolium bromide (MTT) assays. DPP-S NPs showed good biocompatibility

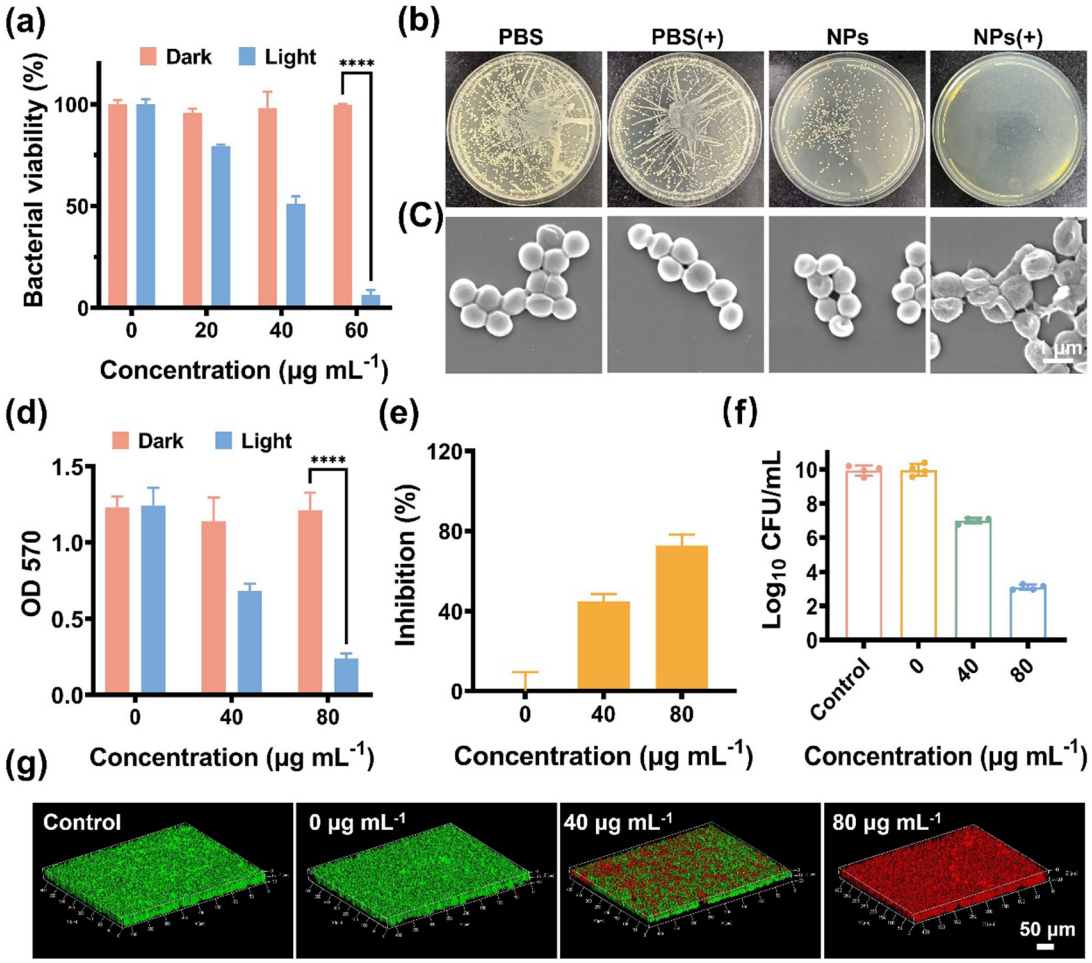

Fig. 4 Antimicrobial properties of DPP-S NPs against MRSA. (a) Survival rate of MRSA. (b) Images of representative agar plates of MRSA after different treatments. (c) SEM images of MRSA after different treatments. (d) OD 570 values of crystal violet staining solutions of different treatment groups. (e) Inhibition rates of MRSA biofilms by DPP-S NPs. (f) Quantitative analysis of bacteria in biofilm after different treatments. (g) 3D confocal laser scanning microscopy images of MRSA biofilms after different treatments.

with cell viabilities above 80% at all concentrations (0–100 μg mL^{-1}) tested (Fig. 6(a)). The body weights of the mice showed an increasing trend after treatment, and the histological structures of the major organs (heart, liver, spleen, lungs, and kidneys) remained normal (Fig. 6(b) and (c)). In addition, routine blood parameters ((white blood cells (WBCs), red blood cells (RBCs), hemoglobin (HGB), and mean corpuscular volume (MCV)) and biochemical indexes ((glutamic–pyruvic aminotransferase (ALT), glutamic–oxaloacetic aminotransferase (AST), blood urea nitrogen (BUN), and creatinine (CREA)) were measured on day 7, which indicated that DPP-S NPs had no obvious effect on the hemopoietic system, liver function, and kidney function (Fig. 6(d)). These results indicate that DPP-S NP-treated mice have good biosafety.

Conclusion

In conclusion, we introduced various groups based on DPP and found that its absorption spectrum was significantly red-shifted. This DPP derivative with NIR absorption was confirmed to have excellent photothermal properties. DPP-S NP-mediated photothermal treatment showed a good killing effect against *S. aureus* and *E. coli*. More importantly, it has the same apparent inhibitory effect on MRSA. In the MRSA-induced wound infection model, the DPP-S NP-mediated photothermal effect effectively inhibited bacterial growth and accelerated the wound healing process. These results indicate that this NIR photothermal material has considerable potential in the treatment of MRSA-induced infections and is expected to play an important role in clinical applications.

Experiments

Preparation of DPP-S NPs

DPP-S (1 mg) and DSPE-PEG_{2000} (5 mg) were completely dissolved in tetrahydrofuran and then slowly added dropwise to deionised water, and DPP-S NPs were obtained through stirring and dialysis.

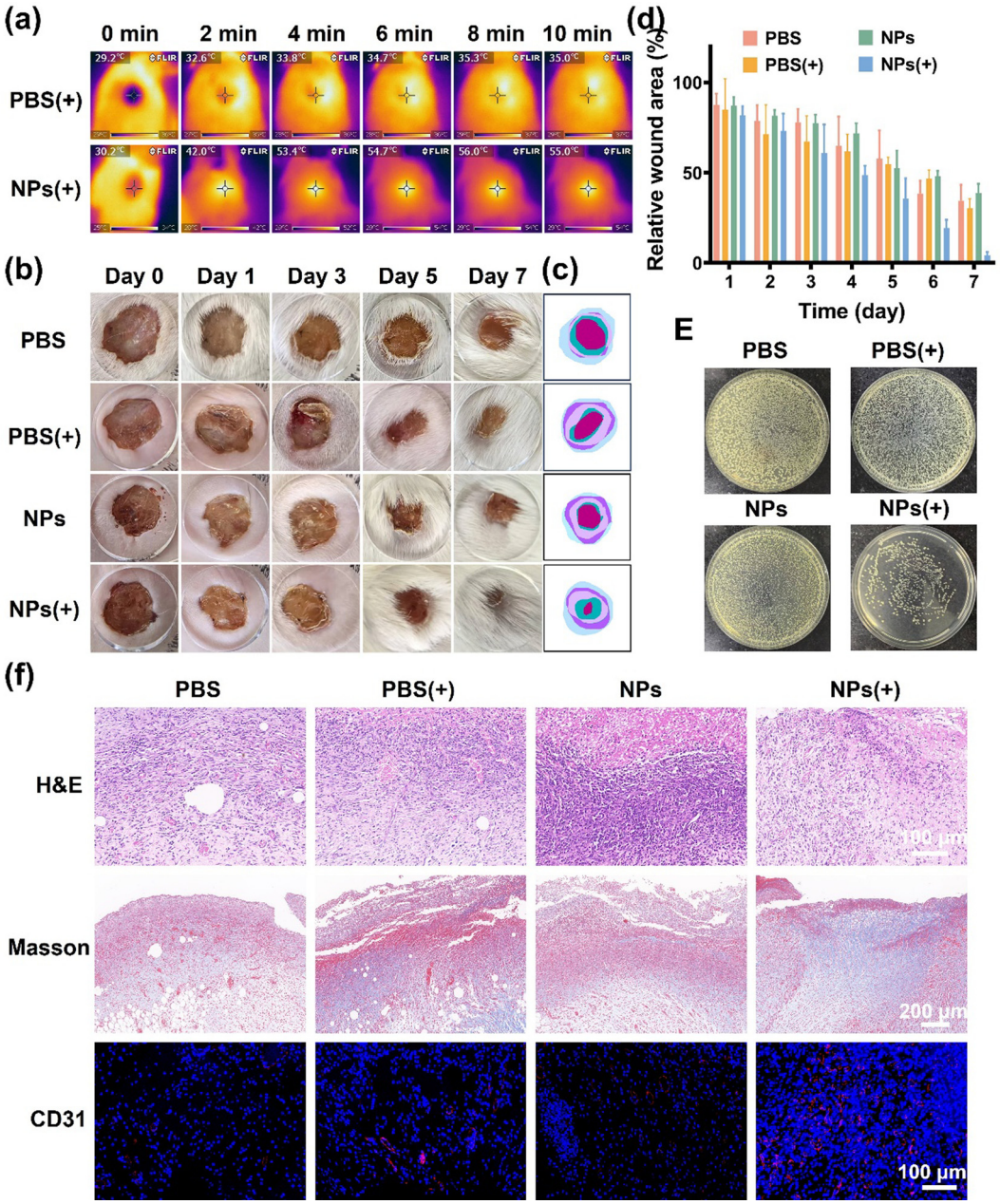

Fig. 5 Antibacterial ability of DPP-S NPs *in vivo*. (a) Changes of wound temperatures during illumination. (b) Photographs of the wounds of the mice under various treatments on the 0, 1st, 3th, 5th, and 7th days. (c) Simulated wound images on different times during treatments. (d) Relative wound areas during the treatment processes. (e) Agar plates of residual bacteria in wounds. (f) H&E, Masson, and CD31 staining of the wounds after different treatments.

Photothermal properties of DPP-S NPs

To evaluate the photothermal behavior of DPP-S NPs, temperature-time curves and images were recorded. First, different concentrations of NPs (20, 40, 60 and 80 μg mL^{-1}) were exposed to 0.6 W cm^{-2} of NIR laser (730 nm). Next, the NPs (80 μg mL^{-1}) were exposed to NIR light (730 nm) with power densities of 0.4, 0.6, and 0.8 W cm^{-2}. Finally, the NPs (80 μg mL^{-1}) were exposed to NIR light (730 nm, 0.6 W cm^{-2}) for five heating–cooling cycles to study their stability. All data were collected every 10 s using an infrared thermal imager. The photothermal conversion efficiency was calculated using the following formula:[41]

$$\eta = \frac{hS(T_{max} - T_{surr}) - Q_o}{I(1 - 10^{-A_{730}})} \quad (1)$$

$$\tau_s = \frac{C_d m_d}{hS} \quad (2)$$

$$Q_o = hS(T_{max,water} - T_{surr}) \quad (3)$$

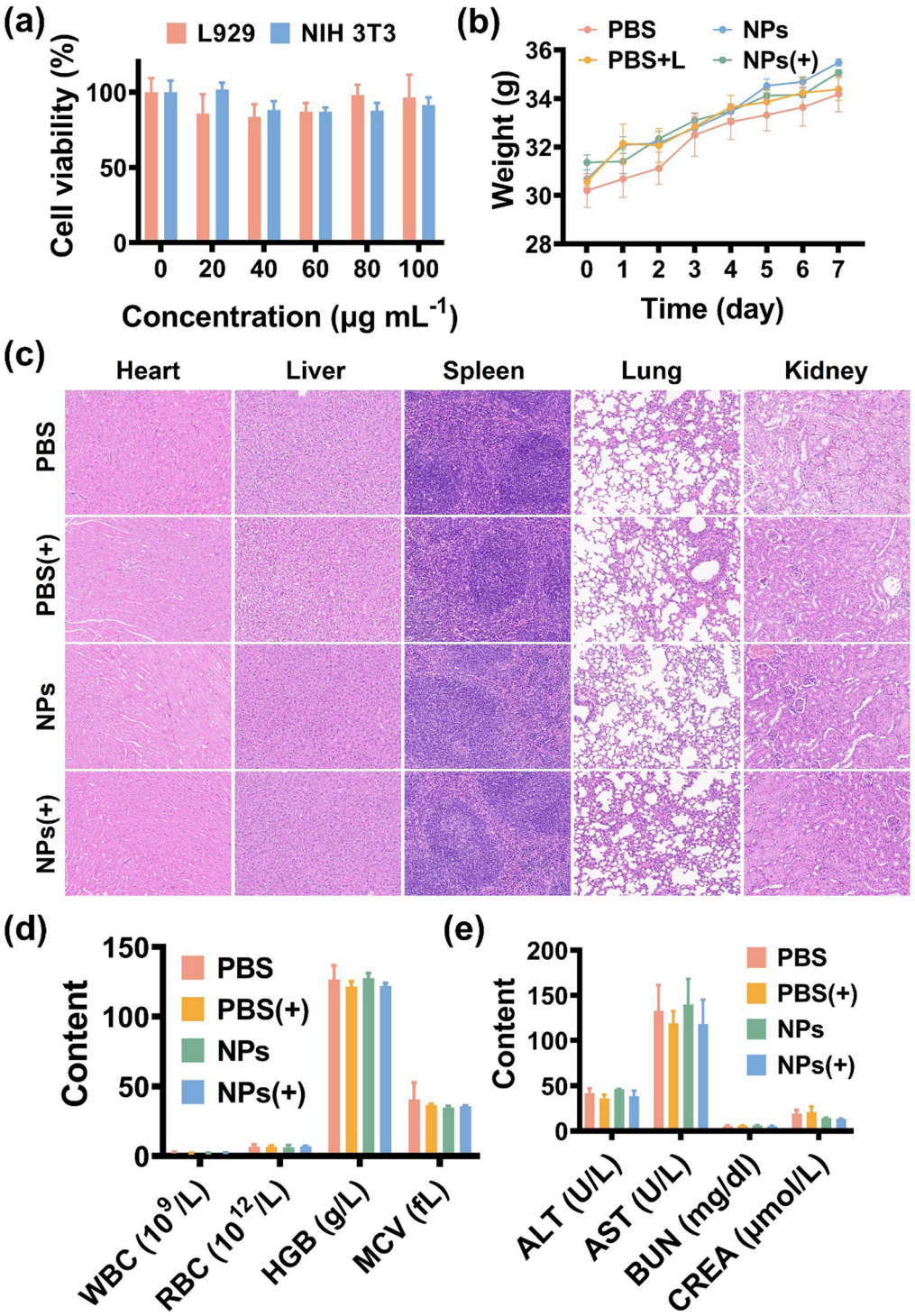

Fig. 6 Biological safety of DPP-S NPs. (a) Cytotoxicity of DPP-S NPs. (b) Changes in the body weights of the mice. (c) H&E staining of sections of major organs of the mice in various groups. (d) Blood routine parameters in each group of mice. (e) Biochemical indexes in various groups of mice.

τ_s can be calculated from the linear regression curve in the cooling curve. m_d and C_d represent the mass of the solution (above 0.4 g) and heat capacity (4.2 J g^{-1} K^{-1}), respectively. $T_{max,water}$ and T_{surr} represent the maximum temperature of water and the ambient room temperature, respectively. T_{max} represents the maximum temperature of the DPP-S NP solution, while I and A_{730} denote the laser power (0.6 W cm^{-2}) and absorbance of DPP-S NPs at 730 nm, respectively.

Bacterial culture

Individual colonies of *S. aureus*, *E. coli*, and MRSA on agar plates were transferred to 3 mL of Luria-Bertani (LB) broth

medium and shaken for 8 h at 37 °C. The bacteria were harvested and washed twice with phosphate-buffered saline (PBS). Then, the bacteria were diluted with PBS to 10^9 CFU mL^{-1} (optical density at 600 nm (OD600 = 1.0)).

Minimum inhibitory concentration (MIC)

Different concentrations of DPP-S NPs and bacterial suspension were incubated in an incubator at 37 °C for 30 min, followed by irradiation with or without laser (0.6 W cm^{-2}) for 10 min, and the survival rate of bacteria was calculated after 24 h of culture in an incubator at 37 °C.

In vitro inhibition of biofilms

Bacterial suspensions at a final concentration of 10^7 CFU mL^{-1} were incubated with DPP-S NPs at different concentrations for 30 min at 37 °C. The samples were irradiated with or without NIR laser for 10 min, followed by incubation at 37 °C for 24 h in an incubator. The medium was removed from the well plates, and each well was washed with PBS to remove planktonic bacteria. The wells were then stained with 0.1% crystal violet for 30 min, rinsed three times with PBS, dried, and photographed. Finally, glacial acetic acid solution was added and allowed to stand for 5 min. The OD570 value was measured to evaluate the degree of biofilm inhibition by DPP-S NPs.

Live/dead staining assay

The bacterial suspension was diluted to 10^7 CFU mL^{-1} and cultured in an incubator at 37 °C for 48 h. After rinsing twice with PBS, the NPs or PBS were added, followed by laser (0.6 W cm^{-2}) irradiation, or no irradiation, for 10 min. The SYTO/PI staining solution was added, and the survival of bacteria in the biofilms was observed using CLSM.

In vitro cytocompatibility of DPP-S NPs

Mouse fibroblast (L929) and embryonic fibroblast (NIH 3T3) cells were inoculated into 96-well plates and cultured in a DMEM medium containing 10% fetal bovine serum at 37 °C in a 5% CO_2 incubator. Various concentrations of NPs were then added, followed by MTT solution after 24 h and DMSO solution after 4 h. The OD values of each well were measured.

In vivo infected wound healing evaluation

All animal experiments were approved by the Ethics Committee of the Changchun Institute of Applied Chemistry, Chinese Academy of Sciences (approval number: 2024-00104).

Healthy Kunming mice were randomly divided into a PBS group, PBS-combined-laser irradiation group (PBS(+)), DPP-S NP group (NPs), and NPs(+) group. All mice were anesthetized, their backs were shaved, and a full circular trauma (1 cm in diameter) was created on the back of each mouse. MRSA (1×10^8 CFU mL^{-1}, 50 μL) was applied to the wounds. After 24 h, the nanoparticle solution or an equivalent amount of PBS was applied to the wounds. The infected wounds were irradiated with a laser (0.6 W cm^{-2}, 730 nm) for 10 min, and the temperature of the wounds was monitored using an infrared thermal imager. Photographs were taken to record changes in the wound area. All mice were euthanized on day 7, and wound tissues and organs (heart, liver, spleen, lung, and kidney) were fixed with 4% paraformaldehyde. Histopathological methods, such as hematoxylin and eosin (H&E), Masson and CD31 immunofluorescence staining, were used to further evaluate wound healing.

Author contributions

Qijia Sun: methodology, investigation, writing – original draft. Xijia Zhou: investigation. Ke Wang: resources, supervision. Tingting Sun: conceptualization, resources, supervision. Zhigang Xie: conceptualization, resources, supervision.

Conflicts of interest

The authors declare that they have no known competing financial interests or personal relationships that could have appeared to influence the work reported in this paper.

Data availability

The data supporting this article have been included as part of the SI.

All relevant experimental data and characterization details are provided in the SI. See DOI: **https://doi.org/10.1039/d5tb01048a**

Acknowledgements

This study was supported by the Disciplinary Crossing and Integration and innovation Project of Norman Bethune Health Science Center of Jilin University (2022JBGS07), Research and Development of Key Medical Technologies of Jilin Science and Technology Department (20240305080YY), and Jilin Provincial Natural Science Foundation Provincial-Local-Enterprise Joint Fund (Group B) (YDZJ202501ZYTS317).

References

1 L. Yang, D. Zhang, W. Li, H. Lin, C. Ding, Q. Liu, L. Wang, Z. Li, L. Mei, H. Chen, Y. Zhao and X. Zeng, *Nat. Commun.*, 2023, **14**, 7658.
2 T. Wang, Y. Li, E. J. Cornel, C. Li and J. Du, *ACS Nano*, 2021, **15**, 9027–9038.
3 M. Dai, W. Ouyang, Y. Yu, T. Wang, Y. Wang, M. Cen, L. Yang, Y. Han, Y. Yao and F. Xu, *J. Adv. Res.*, 2024, **62**, 143–154.
4 J. A. Grousd, H. E. Rich and J. F. Alcorn, *Clin. Microbiol. Rev.*, 2019, **32**, 00107–00118.
5 W. Liu, R. Gao, C. Yang, Z. Feng, W. Ou-Yang, X. Pan, P. Huang, C. Zhang, D. Kong and W. Wang, *Sci. Adv.*, 2022, **8**, eabn7006.
6 X. Hu, H. Zhang, Y. Wang, B.-C. Shiu, J.-H. Lin, S. Zhang, C.-W. Lou and T.-T. Li, *Chem. Eng. J.*, 2022, **450**, 138129.

7 C. Elian, R. Méallet and D.-L. Versace, *Adv. Funct. Mater.*, 2024, **34**, 2407228.
8 X. Qi, Y. Xiang, E. Cai, X. Ge, X. Chen, W. Zhang, Z. Li and J. Shen, *Coordin. Chem. Rev.*, 2023, **496**, 215426.
9 Y. Chen, Y. Gao, Y. Chen, L. Liu, A. Mo and Q. Peng, *J. Controlled Release*, 2020, **328**, 251–262.
10 S. Zhang, A. Wu, A. Ouyang, G. Lian, G. Ma, L. Wang, H. Guo, D. Zhang, J. Jiang and W. Liu, *J. Mater. Chem. B*, 2025, 5403–5416.
11 T. Y. Wang, X. Y. Zhu and F. G. Wu, *Bioact. Mater.*, 2023, **23**, 129–155.
12 J. Peng, K. Du, J. Sun, X. Yang, X. Wang, X. Zhang, G. Song and F. Feng, *Angew. Chem., Int. Ed.*, 2023, **62**, e202214991.
13 X. Bi, Q. Bai, M. Liang, D. Yang, S. Li, L. Wang, J. Liu, W. W. Yu, N. Sui and Z. Zhu, *Small*, 2022, **18**, e2104160.
14 S. Guan, S. Chen, X. Zhang, H. Zhang, X. Liu, Z. Hou, F. Wang, S. Qian, H. Zhu, J. Tan and X. Liu, *Adv. Funct. Mater.*, 2024, **34**, 2316093.
15 P. Manivasagan, T. Thambi, A. Joe, H.-W. Han, S.-H. Seo, Y. Jun Jeon, J. Conde and E.-S. Jang, *Prog. Mater. Sci.*, 2024, **144**, 101292.
16 J. Huo, Q. Jia, H. Huang, J. Zhang, P. Li, X. Dong and W. Huang, *Chem. Soc. Rev.*, 2021, **50**, 8762–8789.
17 F. Cui, T. Li, D. Wang, S. Yi, J. Li and X. Li, *J. Hazard. Mater.*, 2022, **431**, 128597.
18 F. Song, A. Ye, Y. Lu, R. Feng, S. Huang, X. Du, T. Dong, P. Huang, L. Li, L. Yang, J. Zhang, M. Xu, L. Cheng and J. Xiao, *Mater. Today Bio*, 2025, **30**, 101439.
19 J. Sheng, Z. Zu, J. Qi, Y. Zhang, H. Wu, Z. Wang, Y. Miao, T. Zheng, S. Wang, L. Zhang, G. Lu and L. Zhang, *Chem. Eng. J.*, 2024, **485**, 149882.
20 W. Wang, G. Zhang, Y. Wang, J. Ran, L. Chen, Z. Wei, H. Zou, Y. Cai and W. Han, *J. Nanobiotechnol.*, 2023, **21**, 367.
21 P. Zhao, Y. Zhang, X. Chen, C. Xu, J. Guo, M. Deng, X. Qu, P. Huang, Z. Feng and J. Zhang, *Adv. Sci.*, 2023, **10**, e2206585.
22 L. Mei, Y. Zhang, K. Wang, S. Chen and T. Song, *Mater. Today Bio*, 2024, **29**, 101354.
23 L. E. Theune, J. Buchmann, S. Wedepohl, M. Molina, J. Laufer and M. Calderon, *J. Controlled Release*, 2019, **311–312**, 147–161.
24 J. Li, W. Zhang, W. Ji, J. Wang, N. Wang, W. Wu, Q. Wu, X. Hou, W. Hu and L. Li, *J. Mater. Chem. B*, 2021, **9**, 7909–7926.
25 H. Fu, K. Xue, Y. Zhang, M. Xiao, K. Wu, L. Shi and C. Zhu, *Adv. Sci.*, 2023, **10**, e2206865.
26 Q. Ma, X. Sun, W. Wang, D. Yang, C. Yang, Q. Shen and J. Shao, *Chin. Chem. Lett.*, 2022, **33**, 1681–1692.
27 X. Jiang, L. Wang, H. Tang, D. Cao and W. Chen, *Dyes Pigm.*, 2020, **181**, 108599.
28 G. Xu, Y. Song, H. Jin, P. Shi, Y. Jiao, F. Cao, J. Pang, Y. Sun, L. Fang, X. H. Xia and J. Zhao, *Adv. Sci.*, 2024, e2407727.
29 L. Feng, C. Li, L. Liu, Z. Wang, Z. Chen, J. Yu, W. Ji, G. Jiang, P. Zhang, J. Wang and B. Z. Tang, *ACS Nano*, 2022, **16**, 4162–4174.
30 S. Li, Q. Deng, Y. Zhang, X. Li, G. Wen, X. Cui, Y. Wan, Y. Huang, J. Chen, Z. Liu, L. Wang and C. S. Lee, *Adv. Mater.*, 2020, **32**, e2001146.
31 A. Tang, C. Zhan, J. Yao and E. Zhou, *Adv. Mater.*, 2017, **29**, 278299.
32 W. Zou, Y. Zhu, C. Gu, Y. Miao, S. Wang, B. Yu, Y. Shen and H. Cong, *J. Mater. Sci.*, 2020, **55**, 9918–9947.
33 L. Yuan, Y. Su, B. Yu, Y. Shen and H. Cong, *Biomater. Sci.*, 2023, **11**, 985–997.
34 F. Bu, X. Kang, D. Tang, F. Liu, L. Chen, P. Zhang, W. Feng, Y. Yu, G. Li, H. Xiao and X. Wang, *Bioact. Mater.*, 2024, **33**, 341–354.
35 X. Cheng, C. Zhang, K. Shen, H. Liu, C. Bai, Q. Ding, M. Guan, J. Wu, Z. Tian, D. Chen, L. Cai, X. Hong and Y. Xiao, *Chem. Eng. J.*, 2022, **446**, 136929.
36 C. Li, W. Zhang, S. Liu, X. Hu and Z. Xie, *ACS Appl. Mater. Interfaces*, 2020, **12**, 30077–30084.
37 X. Yu, J. Zhao, X. Ma and D. Fan, *Chem. Eng. J.*, 2023, **465**, 142933.
38 F. W. Xia, B. W. Guo, Y. Zhao, J. L. Wang, Y. Chen, X. Pan, X. Li, J. X. Song, Y. Wan, S. Feng and M. Y. Wu, *Adv. Mater.*, 2023, **35**, e2309797.
39 S. G. V. Charlton, A. N. Bible, E. Secchi, J. L. Morrell-Falvey, S. T. Retterer, T. P. Curtis, J. Chen and S. Jana, *Adv. Sci.*, 2023, **10**, e2207373.
40 D. Xian, R. Luo, Q. Lin, L. Wang, X. Feng, Y. Zheng, L. Lin, J. Chi, Y. Yan, G. Quan, T. Peng, Z. Xu, C. Wu and C. Lu, *Mater. Today Bio*, 2025, **31**, 101498.
41 X. Duan, J. Li, S. Huang, A. Li, Y. Zhang, Y. Xue, X. Song, Y. Zhang, S. Hong, H. Gao, Z. Wu and X. Zhang, *Chem. Eng. J.*, 2023, **477**, 146937.

